JOURNAL OF THERMOPHYSICS AND HEAT TRANSFER
Vol. 15, No. 3, July–September 2001

Heat Transfer in a Channel with Dimples and Protrusions on Opposite Walls

Gazi I. Mahmood,* Mounir Z. Sabbagh,* and Phillip M. Ligrani†
University of Utah, Salt Lake City, Utah 84112-9208

Local and spatially averaged Nusselt-number data are presented for the dimpled surface of a channel, both with and without protrusions (with the same shapes as the dimples) on the opposite wall. Channel aspect ratio is 16, ratio of channel height to dimple print diameter is 0.5, Reynolds numbers based on channel height ranges from 5×10^3 to 3.5×10^4, and ratio of channel inlet stagnation temperature to wall temperature ranges from 0.73 to 0.94. Because of the added vortical, secondary flow structures and flow unsteadiness induced by the protrusions, local and spatially averaged Nusselt numbers are augmented considerably and have greater Reynolds-number dependence, compared to a channel with a smooth top wall and dimples on one opposite wall. Nusselt-number variations are also observed as the location of the array of protrusions is changed with respect to the dimples. Form drag and channel friction factors are augmented, and thermal performance factors are then generally lower when protrusions are employed, compared to a channel with a smooth top surface and a dimpled bottom surface.

Nomenclature

D	=	dimple print diameter
f	=	channel friction factor
f_0	=	baseline friction factor in channel measured with smooth top and bottom channel surfaces
H	=	channel height
k	=	thermal conductivity
Nu	=	Nusselt number based on channel hydraulic diameter
Nu_0	=	baseline Nusselt number based on channel hydraulic diameter and measured with smooth top and bottom channel surfaces
Re_{Dh}	=	Reynolds number based on bulk mean channel velocity and channel hydraulic diameter
Re_H	=	Reynolds number based on bulk mean channel velocity and channel height
T_{oi}	=	spatially averaged stagnation temperature at test section inlet
T_w	=	surface temperature
X	=	streamwise coordinate measured from upstream edge of test surface
Z	=	spanwise coordinate measured from spanwise centerline of test surface

Superscripts

$\bar{}$	=	spanwise averaged or streamwise averaged
$=$	=	globally averaged over a surface area

I. Introduction

MUCH attention is devoted to the development of heat transfer augmentation devices for internal passages. Rib turbulators, arrays of pin fins, and, more recently, passage surfaces with arrays of dimples are employed for this purpose. This is because improvements in augmentation levels are useful in a variety of practical applications, including macro- and microscale heat exchangers, electronics cooling, combustion chamber liners, and passages for internal cooling of turbine airfoils in gas turbine engines. The present paper is focused on the use of dimples on one surface of a channel with an aspect ratio of 16. Here, local and global surface heat transfer are augmented compared to a smooth surface by the reattachment of the shear layer, which forms across the top of each dimple, as well as the vortex structures and vortical fluid shed from each individual dimple indentation, which then advect over the flat surface just downstream.[1] In contrast, pressure drops and friction factors are not increased appreciably (compared to a channel with all smooth surfaces) because no form drag is produced by objects protruding into the flow.[2] The use of dimples on the surfaces of internal passages is thus advantageous because 1) high heat transfer augmentations are obtained,[1] 2) pressure drops are relatively small,[2] 3) manufacturing dimpled surfaces is easier than manufacturing surfaces with other types of augmentation devices, and 4) their use does not add significant extra material and weight to surfaces.

Early surface heat transfer studies from Russia employ flows over flat walls with regular arrays of spherical pits,[3] flows in annular passages with a staggered array of concave dimples on the interior cylindrical surface,[4] flows in single hemispherical cavities,[5,6] flows in diffuser and convergent channels each with a single hemispherical cavity,[7] and flows in a narrow channel with spherically shaped dimples placed in relative positions on two opposite surfaces.[8] Heat transfer augmentations as high as 150%, compared to smooth surfaces, are reported, sometimes with appreciable pressure losses.[4]

More recently, Chyu et al.[9] presented data on the influences of Reynolds number on local heat transfer coefficient distributions on surfaces imprinted with staggered arrays of two different shapes of concavities. In some cases enhancement of the overall heat transfer rate is about 2.5 times smooth surface values over a range of Reynolds numbers, and pressure losses are about half the values produced by conventional rib turbulators. Lin et al.[10] present computational simulation results of the flow structures, flow streamlines, temperature distributions, and resulting surface heat transfer distributions for the same geometries and flow conditions. Moon et al.[11] give data that illustrate the effects of channel height on heat transfer and pressure losses on a surface with a staggered pattern of dimples. According to the investigators, improvements in heat transfer intensification and pressure losses remain at approximately constant levels over the ranges of Reynolds number and channel height investigated. Mahmood et al.[1] describe the mechanisms responsible for local and spatially averaged heat transfer augmentations on flat channel surfaces with an array of dimples on one wall. Included are the important influences of the ratio of inlet stagnation temperature to surface temperature, which gives additional surface heat transfer augmentation as its magnitude decreases.

Of interest in the present paper are the use of protrusions on the channel wall placed opposite to the dimpled surface and their effects

Received 25 September 2000; revision received 9 March 2001; accepted for publication 14 March 2001.

*Graduate Student, Convective Heat Transfer Laboratory, Department of Mechanical Engineering.

†Professor, Convective Heat Transfer Laboratory, Department of Mechanical Engineering, 50 S. Central Campus Drive, MEB 2202.

in further augmenting dimple surface heat transfer levels. The protrusions aid this process as continuity causes greater quantities of fluid to be ejected from each dimple.[2] Because the mixing in the flow is also increased, this occurs with greater turbulence transport levels.[2] The issue that is then considered is the amount of additional heat transfer augmentation produced, in comparison with the increase in channel friction factors resulting from protrusion form drag. To address this, local and spatially averaged Nusselt-number data and thermal performance factors are presented for the dimpled surface of a channel, both with and without protrusions (with the same shapes as the dimples) on the opposite wall. Channel aspect ratio is 16, ratio of channel height to dimple print diameter is 0.5, Reynolds numbers based on channel height ranges from 5×10^3 to 3.5×10^4, and ratio of channel inlet stagnation temperature to wall temperature ranges from 0.73 to 0.94.

II. Experimental Apparatus and Procedures

A. Channel for Heat Transfer Measurements

A schematic of the facility used for heat transfer measurements is shown in Fig. 1. The air used within the facility is circulated in a closed loop. One of two circuits is employed, depending upon the Reynolds number and flow rate requirements in the test section. For Reynolds numbers Re_H less than 2×10^4, a 102-mm pipe is connected to the intake of an ILG Industries 10P-type centrifugal blower. For higher Reynolds numbers a 203-mm pipe is employed with a New York Blower Co. 7.5 HP, size 1808 pressure blower. In each case the air mass flow rate from the test section is measured (upstream of which ever blower is employed) using an American Society of Mechanical Engineers (ASME) standard orifice plate and Validyne M10 digital pressure manometer. The blower then exits into a series of two plenums (0.9 m square and 0.75 m square). A Bonneville crossflow heat exchanger is located between two of these plenums and is cooled with liquid nitrogen at flow rate appropriate to give the desired air temperature at the exit of the heat exchanger. As the air exits the heat exchanger, it enters the second plenum, from which the air passes into a rectangular bell mouth inlet, followed by a honeycomb, two screens, and a two-dimensional 19.5 to 1 contraction ratio nozzle. This nozzles leads to a rectangular cross section, 411 mm by 25.4 mm inlet duct, which is 1219 mm in length. This is equivalent to 25.4 hydraulic diameters (where hydraulic diameter is 47.8 mm). A trip is employed on the bottom surface of the inlet duct, just upstream of the test section, which follows with the same cross-section dimensions. Test-section aspect ratio is then about 16. The test-section duct exits to a 0.60-m square plenum, which is followed by two pipes, each containing an orifice plate, mentioned earlier. The bottom surface of the test section is dimpled, and either a smooth surface or a surface with protrusions can be employed on the top wall.

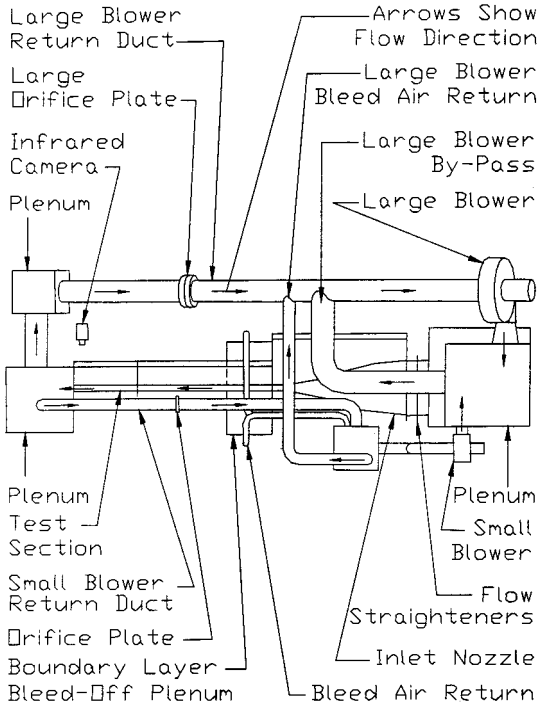

Fig. 1 Experimental facility for heat transfer measurements.

All exterior surfaces of the facility (between the heat exchanger and test section) are insulated with Styrofoam ($k = 0.024$ W/mK) or two to three layers of 2.54 cm thick, Elastomer Products black neoprene foam insulation ($k = 0.038$ W/mK) to minimize heat losses. Calibrated copper-constantan thermocouples are located between the three layers of insulation located beneath the test section to determine conduction losses. Between the first layer and the 3.2-mm-thick acrylic, dimpled test surface is a custom-made Electrofilm etched-foil heater (encapsulated between two thin layers of Kapton) to provide a constant heat-flux boundary condition on the test surface. The acrylic surface contains 24 copper-constantan thermocouples and is adjacent to the airstream. Each of these thermocouples is located 0.0508 cm just below this surface to provide measurements of local surface temperatures, after correction for thermal contact resistance and temperature drop through the 0.0508 cm thickness of acrylic. Acrylic is chosen because of its low thermal conductivity ($k = 0.16$ W/mK at 20°C) to minimize streamwise and spanwise conduction along the test surface and thus minimize "smearing" of spatially varying temperature gradients along the test surface. Acrylic also works well for infrared imaging because, when painted flat black, its surface emissivity ranges from 0.80 to 0.90.

B. Test Surface Geometry Details

Figures 2a–2d present the geometric details of the test surface, including dimple and protrusion geometries. A total of 13 rows of dimples are employed in the streamwise direction, and nine rows are employed in the spanwise direction in a staggered array on the bottom wall. The same arrangement is employed for the protrusions on the top surface (except that the protrusions protrude into the flow). The protrusions are positioned with respect to the dimples in two different ways. With configuration 1, or the full offset configuration, the protrusions and dimples are misaligned with each other with a streamwise distance between centers of 4.11 cm. With configuration 2, no offset is employed, and the protrusions and dimples are exactly aligned with each other. Also identified in Fig. 2a is the test-section coordinate system employed for the study.

C. Local Nusselt-Number Measurement

The power to the foil heater is controlled and regulated using a variac power supply. Energy balances, performed on the heated test surface, then allow determination of local magnitudes of the convective heat flux. To determine this surface heat flux (used to calculate heat transfer coefficients), the convective power provided by the etched foil heater is divided by the total area of the test surface (flat portions and dimples). Thus, local heat transfer coefficients and local Nusselt numbers can be considered to be based on the same area. The mixed-mean temperature of the air entering the test section is measured using five calibrated copper-constantan thermocouples spread across its cross section. Energy balances are then used to determine the local mixed mean temperature through the test section. All measurements are obtained when the test facility is at steady state, achieved when each of the temperatures from the 24 thermocouples (on the test surface) vary by less than 0.1°C over a 10-min period.

Spatially resolved temperature distributions along the dimpled test surface are determined using infrared imaging in conjunction with thermocouples, energy balances, digital image processing, and in situ calibration procedures. To accomplish this, the infrared radiation emitted by the heated interior surface of the channel is captured using a VideoTherm 340 Infrared Imaging Camera, which operates at infrared wave lengths from 8 to 14 μm. Temperatures, measured using the calibrated, copper-constantan thermocouples distributed

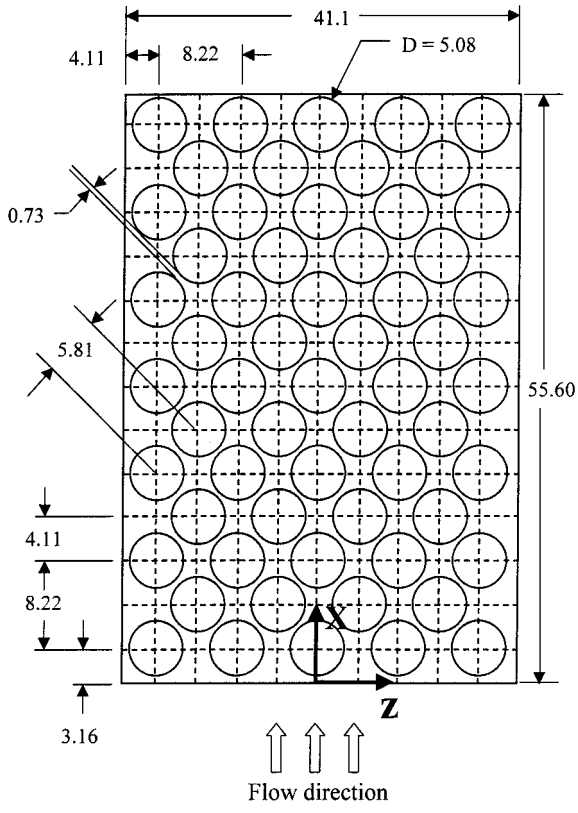

a) Overall geometry of dimpled test surface or dimpled top wall, including coordinate system

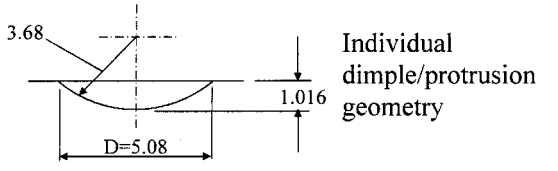

b) Individual dimple/protrusion geometry

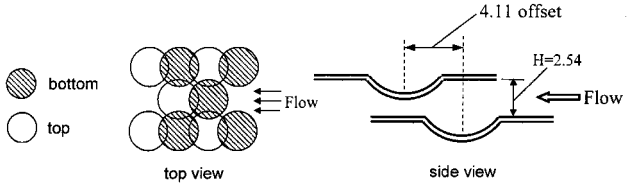

Configuration 1, protrusions and dimples misaligned.

c) Configuration 1 arrangement with dimples and protrusions misaligned with full offset between centers

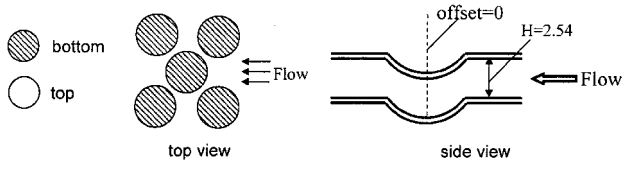

Configuration 2, protrusions and dimples aligned.

d) Configuration 2 arrangement with dimples and protrusions aligned with no offset between centers

Fig. 2 Detail of test section surfaces.

along the test surface adjacent to the flow, are used to perform the in situ calibrations simultaneously as the radiation contours from surface temperature variations are recorded.

This is accomplished as the camera views the test surface through a custom-made, zinc-selenide window (which transmits infrared wavelengths between 6 and 17 μm) located on the top wall of the test section. Reflection and radiation from surrounding laboratory sources are minimized using an opaque shield, which covers the camera lens and the zinc-selenide window. Frost buildup on the outside of the window is eliminated using a small heated airstream. The window is located just above the tenth to thirteenth rows of dimples downstream from the leading edge of the test surface. Five to six thermocouple junction locations are usually present in the infrared field viewed by the camera. The exact spatial locations and pixel locations of these thermocouple junctions and the coordinates of a 12.7 by 12.7-cm field of view are known from calibration maps obtained prior to measurements. During this procedure, the camera is focused and rigidly mounted and oriented relative to the test surface in the same way as when radiation contours are recorded. With these data, gray scale values at pixel locations within videotaped images from the infrared imaging camera are readily converted to temperatures.

Images from the infrared camera are recorded as 8-bit gray scale images on commercial videotape using a Panasonic AG-1960 video recorder. Images are then digitized using NIH Image v1.60 software, operated on a Power Macintosh 7500 PC computer. Subsequent software is used to convert each of 256 possible gray scale values to temperature at each pixel location using calibration data. This software then determines values of local Nusselt-numbers. Thermal conductivity in the Nusselt number is based on the average of the local wall temperature and the temperature of the air at the upstream inlet. Nusselt-number length scale is channel hydraulic diameter. Contour plots of local surface temperature and Nusselt number are prepared using DeltaGraph v4.0 software. Each individual image covers a 300 by 300 pixel area. Sargent et al.[12] and Hedlund and Ligrani[13] provide additional details on the infrared imaging and measurement procedures.

The time-averaged data presented are obtained from a time average of 40 instantaneous data sets over a time period of 40 s. To check the effects of not employing protrusions on the zinc-selenide window (located on the top wall so that the infrared camera can view the test surface), surface Nusselt-number distributions are obtained both with and without extra protrusions taped to the window. No differences are apparent in the vicinity of the tenth row of dimples. Only very small differences are apparent (and only for some flow conditions) near the next two rows of dimples located downstream. These are addressed in additional detail later in the paper.

To further check the repeatability and consistency of the results, infrared images from three different regions on the test surface (all located over the tenth, eleventh, and twelfth rows of dimples) are measured. Each of these regions covers the exact same area, which is the same as the center-to-center distance between four adjoining dimples in the tenth and twelfth rows. Results are identical for overlapping regions and repeatable well within uncertainty magnitudes when considered at similar locations with respect to different dimples. This indicates appropriate flow uniformity and periodicity in the test section, as well as correct test surface operation.

D. Uncertainty Estimates

Uncertainty estimates are based on 95% confidence levels and determined using procedures described by Moffat.[14] Uncertainty of temperatures measured with thermocouples is ± 0.15°C. Spatial and temperature resolutions achieved with the infrared imaging are about 0.52 mm and 0.8°C, respectively. This magnitude of temperature resolution is caused by uncertainty in determining the exact locations of thermocouples with respect to pixel values used for the in situ calibration. Local Nusselt-number uncertainty is then about $\pm 6.8\%$ for $T_{oi}/T_w = 0.78$. Corresponding Nusselt-number ratio uncertainty is about ± 0.19 (for a ratio of 2.00) or $\pm 9.6\%$. Such Nu/Nu_0 uncertainties then increase as T_{oi}/T_w becomes larger. Reynolds-number uncertainty is about $\pm 1.7\%$ for Re_H of 10.2×10^3.

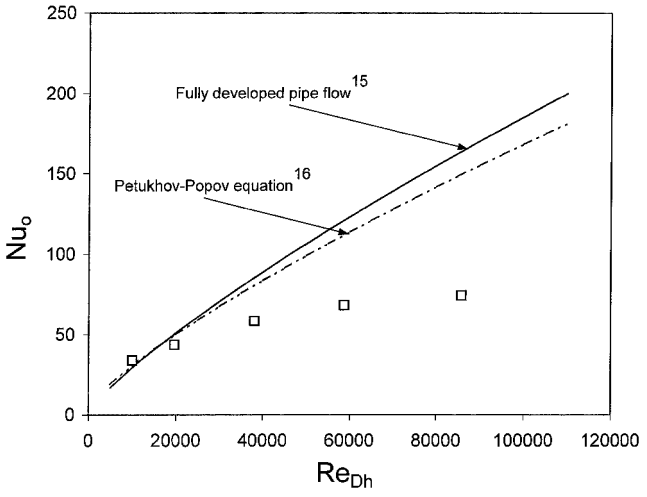

Fig. 3 Comparison of baseline Nusselt numbers with correlations for channel flow and pipe flow.

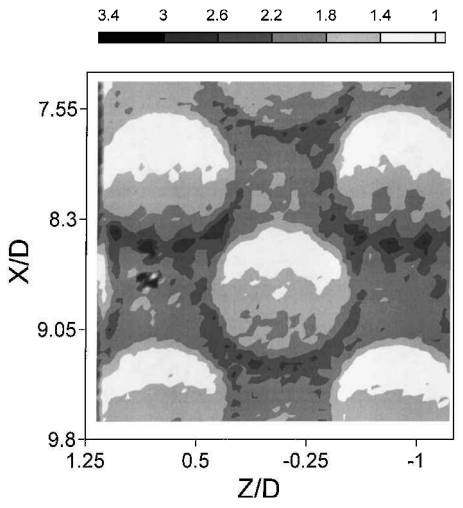

Fig. 4 Local, time-averaged Nusselt-number ratios along the ninth to twelfth dimple rows for $Re_H = 10.2 \times 10^3$, $T_{oi}/T_w = 0.94$, and a smooth top channel surface.

III. Experimental Results and Discussion

A. Baseline Nusselt Numbers

Baseline Nusselt numbers Nu_0 are measured with a smooth test surface replacing the dimpled test surface, also with $H/D = 0.5$, and the same Reynolds numbers as employed in the dimpled channel. Other than the test surface, all geometric characteristics of the channel are the same as when a dimpled test surface is installed. These baseline values are used to normalize dimpled test surface values and are thus used as a basis of comparison to dimpled test surface values. All baseline measurements are made with thermally and hydraulically fully developed channel flow, at a ratio of inlet stagnation temperature to wall temperature T_{oi}/T_w of 0.92–0.94. The variation of baseline Nu_0 values (based on hydraulic diameter) with Reynolds number Re_{Dh} is shown in Fig. 3. Values are in rough agreement with the correlation for circular tubes from Kays and Crawford[15] and the Petukhov–Popov correlation for rectangular cross-section duct flows[16] for $Re_{Dh} < 2 \times 10^4$. Measured values are then lower than these correlations at higher Reynolds numbers, as expected. This is because the correlations are for internal passages with heating around the entire circumference, whereas the rectangular passage in the present experiment is heated only on one flat surface.

B. Spatially Resolved Nusselt Numbers and Flow Structure with a Smooth Top Wall

Figure 4 presents spatially resolved Nusselt numbers measured on the dimpled test surface placed on one wall of the $H/D = 0.5$ channel. The opposite channel wall is smooth, Reynolds number Re_H for the measurements is 10.2×10^3, and $T_{oi}/T_w = 0.94$. Flow direction for the figure is from top to bottom in the direction of increasing X/D. The image shows a Nusselt-number distribution along dimples in the tenth to twelfth rows from the beginning of the test surface. As mentioned, these particular data are obtained from a time average of 40 instantaneous data sets over a time period of 40 s.

The circular concave depressions of the dimples are positioned at the same locations as the circular Nu/Nu_0 contours in Fig. 4. Lower Nusselt-number ratios are located over the upstream halves of the depressions. Local Nusselt-number ratios are then higher in the downstream halves. The highest values are then located near the downstream rims of each dimple, both slightly within each depression, and on the flat surface just downstream of each dimple. Most local values in the concave cavities are higher than values measured a smooth channel at the same Reynolds number and temperature ratio, which is consistent with the results presented by Kesarev and Kozlov[5] and Schukin et al.[7]

The high Nu/Nu_0 region is spread over a region that is approximately parallel to the downstream edge of the dimple, over Z/D from -0.3 to $+0.3$ and over X/D from 9.1 to 9.7. Three fingers from this region then extend downwards in the positive X/D direction, two of which are located near the spanwise edges of adjoining dimples. These two fingers continue to extend downwards in the $+X/D$ direction until they connect with high Nu/Nu_0 regions located on the flat surfaces just downstream of the adjacent dimples. With this arrangement regions of high Nu/Nu_0 are interconnected downstream of and to the sides of most all dimples in the streamwise and spanwise adjacent rows.

According to Mahmood et al.,[1] these regions of high local Nu/Nu_0 are the result of collections of vortex pairs and vortical fluid, which are shed periodically from each dimple. This periodicity takes the form of a repeated cycle of events, where each cycle consists of inrush of fluid to each dimple, followed by outflow and vortex shedding. From visualizations of flow structure at $H/D = 0.5$,[1] the flow, which is shed from each dimple, is primarily in the form of three distinct upwash regions. Each of these regions leads to and is then located between the vortices, which make up a vortex pair. The most prominent of each of these vortex pairs is associated with an upwash region in the streamwise-normal plane located approximately along the centerline of each dimple. The two other vortex pairs and associated upwash regions are located near the diagonal-spanwise edges of each dimple or just downstream of these locations. The heat transfer augmentations, present near downstream rims of dimples as well as on flat surfaces downstream of and between dimples, are then present mostly from 1) the strong secondary fluid motions of these vortex pairs near the surface, 2) the periodicity and unsteadiness of this vortical fluid, 3) the reattachment of the separated shear layer, which advects across the opening of each dimple, and 4) augmented turbulence transport.

C. Spatially Resolved Nusselt Numbers and Flow Structure with Protrusions on Top Wall

When protrusions are added to the top wall, compared to a channel with a smooth top wall, the secondary flows that are present in the channel are present in stronger magnitudes over much larger portions of the channel cross sections.[2] The turbulence intensities and the mixing associated with them are also higher at much lower Reynolds numbers. The obstructions produced by the top wall protrusions, and the resulting effects of continuity, cause the flow to be forced from the dimples on the opposite wall in a similar fashion as then no protrusions are present. However, with the protrusions this occurs with more violence and over greater volumes. The associated vortex structures and packets of vortical fluid shed from the dimples then contain stronger secondary flows and are more unsteadiness,[2] and as a result, local heat transfer augmentations are even higher.

This is illustrated by the results in Fig. 5, which shows local Nusselt-number ratio distributions along dimples from the middle of the tenth to the middle of the thirteenth dimple rows (as counted

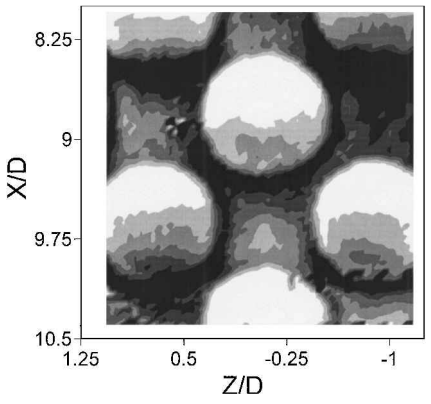

Fig. 5 Local, time-averaged Nusselt-number ratios along the tenth to thirteenth dimple rows for $Re_H = 10.6 \times 10^3$, $T_{oi}/T_w = 0.92$, and configuration 1 (nonaligned) protrusions on the channel top surface. Nu/Nu_0 scale given in Fig. 4.

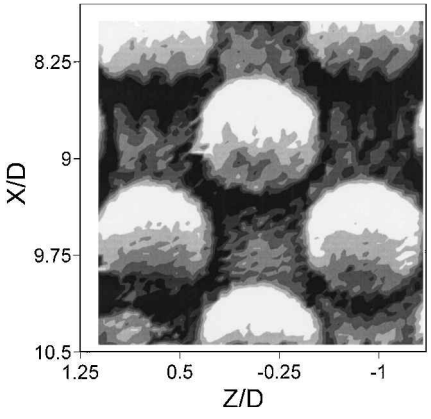

Fig. 6 Local, time-averaged Nusselt-number ratios along the tenth to thirteenth dimple rows for $Re_H = 10.4 \times 10^3$ $T_{oi}/T_w = 0.93$, and configuration 2 (aligned) protrusions on the channel top surface. Nu/Nu_0 scale given in Fig. 4.

from the front of the test surface). Channel height, dimple size, channel aspect ratio, Reynolds number, and temperature ratio are the same as for the results presented in Fig. 4. The only difference is that protrusions are employed on the top wall (to obtain the Fig. 5 results) in a configuration 1 arrangement, which means that the dimples and protrusions are arranged with a "full-offset" so that they are out of phase with each other (Fig. 2c). Comparing the results in Figs. 4 and 5 shows that qualitative Nu/Nu_0 patterns have some similarity; however, quantitative magnitudes are significantly higher in the latter figure. In particular, the belts of locally higher Nu/Nu_0 extend further inside the downstream rims of the dimples when protrusions are employed. In addition, Nu/Nu_0 values decrease slightly on the upstream halves of the dimple cavities with the protrusions. In some cases regions of locally higher Nu/Nu_0, measured with protrusions, are slightly broader downstream of dimple row 10 ($X/D = 8.2$–8.8) than those downstream of dimple row 11 ($X/D = 9.0$–9.5). This is because of the absence of protrusions on the zinc-selenide window over the measurement area and indicates that the protrusions affect the flow in their immediate streamwise vicinity. The same Nu/Nu_0 scales are used for all of the data in Figs. 4–8.

As the relative positions of the dimples and protrusions are changed, the structural characteristics, intensities, and distributions of the vortical structures produced by the dimples are altered further.[2] Figure 6 shows that this results in additional alterations to local Nusselt-number ratio magnitudes. These data are obtained with the protrusions in a configuration 2 arrangement, in which the dimples and protrusions are exactly aligned with each other (Fig. 2d). Otherwise, channel geometry, Reynolds number, temperature ratio (as well as the Nu/Nu_0 scale used to present the data) are the same as for the preceding figure. Qualitative similarity of Nu/Nu_0 patterns

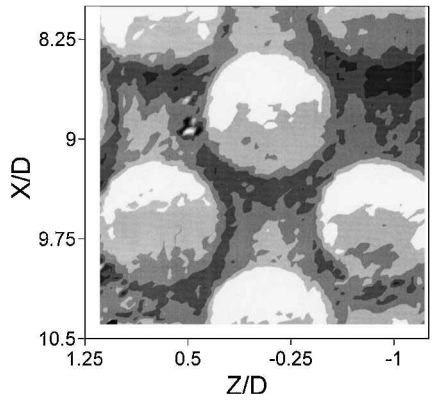

Fig. 7 Local, time-averaged Nusselt-number ratios along the tenth to thirteenth dimple rows for $Re_H = 3.5 \times 10^4$, $T_{oi}/T_w = 0.94$, and configuration 2 (aligned) protrusions on the channel top surface. Nu/Nu_0 scale given in Fig. 4.

with results in the preceding two figures is apparent. However, the highest Nu/Nu_0 magnitudes in Fig. 6 (obtained with aligned protrusions) are slightly lower than the highest magnitudes in Fig. 5 (obtained with full offset protrusions). Three vertical stripes of locally higher Nu/Nu_0 are present, which emanate downstream (and downwards) from each dimple in the tenth row in Fig. 6. These are located at X/D from 8.25 to 9.0 and at Z/D from $+0.35$ to $+1.35$ and at Z/D from -1.35 to -0.35. These are qualitatively similar to Nu/Nu_0 variations present downstream of the tenth row of dimples in Fig. 4. There, stripes of locally higher Nu/Nu_0 are positioned over the same X/D and Z/D ranges as the ones in Fig. 6. In both cases these stripes are caused by the three pairs of vortices, which advect along the flat surface downstream of the dimples.

Figure 7 shows the changes to local Nu/Nu_0 distributions when all geometry and flow conditions are the same as the ones used to obtain the results in Fig. 6, except the Reynolds number Re_H is increased from 10.4×10^3 to 3.5×10^4. Similar qualitative variations are again present; however, local Nu/Nu_0 magnitudes are significantly lower. The same Nu/Nu_0 scale is again employed. Comparing the results in Figs. 6 and 7 indicates that differences are especially apparent in the downstream portions of the dimple cavities and on the flat surfaces downstream of the dimple cavities. This indicates that advection of heat by the bulk flow and the turbulence transport from the three-dimensional unsteady secondary flows produced by the dimples and protrusions change significantly as the bulk fluid velocity in the channel is altered. Smaller alterations to quantitative and qualitative Nu/Nu_0 distributions are observed in the upstream halves of the dimple cavities as Re_H varies. The dimple-protrusion channel arrangement thus produces Nu/Nu_0 values with larger Reynolds-number dependence than if a smooth top wall is employed opposite to the dimpled surface.[1] This is related to the roughness character of the protrusions, especially the mixing and form drag produced by each protrusion element.

The Nusselt-number ratio distributions in Figs. 6 and 8 are for T_{oi}/T_w of 0.93 and 0.78, respectively. The Reynolds numbers for these two data sets are 10.4×10^3 to 13.2×10^3, respectively, which means that values are about the same. Comparing the two contour plots shows that, as the ratio of inlet stagnation temperature to wall temperature decreases, the coolest parts of the test surface, which correspond to the highest values of Nu/Nu_0, intensify, broaden, and extend farther away from the downstream rims of the dimples. These are especially evident to the sides of each dimple and downstream of each dimple in Fig. 8. This becomes more significant as the temperature ratio T_{oi}/T_w decreases because vortex pairs and vortical fluid in the channel bring larger amounts of colder fluid from the central parts of the channel to regions near the dimpled surface. This process is aided by variable property influences and buoyancy.

D. Spatially Averaged Nusselt Numbers

Spanwise-averaged and streamwise-averaged Nusselt numbers are presented in Figs. 9 and 10, respectively. These data are

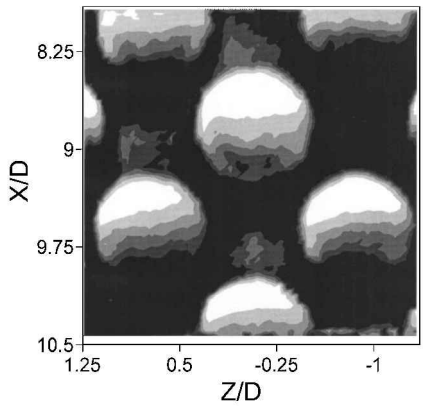

Fig. 8 Local, time-averaged Nusselt-number ratios along the tenth to thirteenth dimple rows for $Re_H = 13.2 \times 10^3$, $T_{oi}/T_w = 0.78$, and configuration 2 (aligned) protrusions on the channel top surface. Nu/Nu_0 scale given in Fig. 4.

	Top Wall	Configuration	Offset	T_{oi}/T_w	Re_H
●	Smooth	—	—	0.94	10,200
◇	Protrusions	1	Full offset (Misaligned)	0.92	10,600
□	Protrusions	2	No offset (Aligned)	0.93	10,400
△	Protrusions	2	No offset (Aligned)	0.94	35,000
■	Protrusions	2	No offset (Aligned)	0.78	13,200

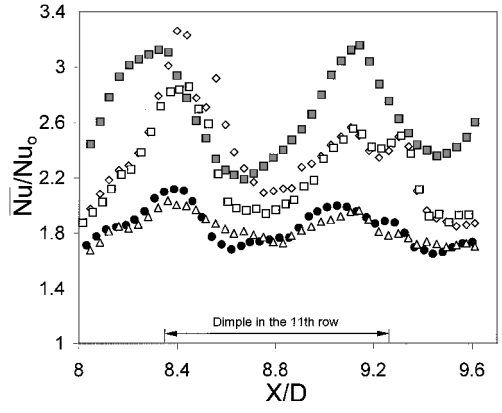

Fig. 9 Spanwise-averaged Nusselt-number ratios as dependent on X/D for different Reynolds numbers Re_H and temperature ratios T_{oi}/T_w.

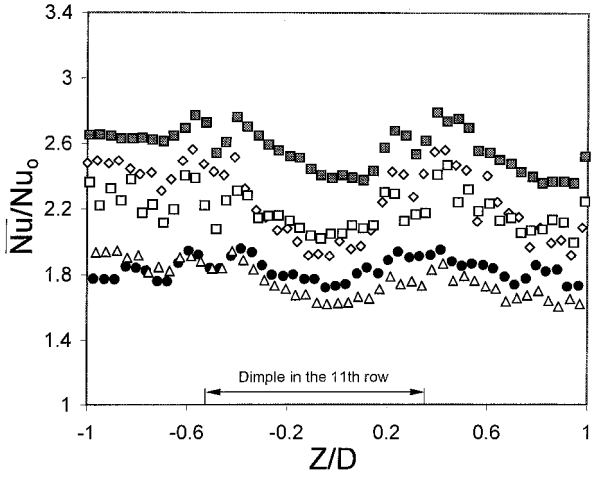

Fig. 10 Streamwise-averaged Nusselt-number ratios as dependent on Z/D for different Reynolds numbers Re_H and temperature ratios, T_{oi}/T_w. Symbols identified in Fig. 9.

presented for different Reynolds numbers, temperature ratios, and protrusion-wall positions. Also included is a data set measured with a smooth, undimpled top wall for $Re_H = 10.2 \times 10^3$ and T_{oi}/T_w of 0.94. To obtain the data presented in Fig. 9, local Nu/Nu_0 values at a constant X/D location are averaged to determine spanwise-averaged $\overline{Nu}/Nu_0$ magnitudes at that X/D location. To obtain the data given in Fig. 10, local Nu/Nu_0 are averaged at constant Z/D locations to obtain streamwise-averaged $\overline{Nu}/Nu_0$ at the same Z/D locations. In each case, spatial averages are obtained over a rectangular area from the center to center of adjacent dimples in the tenth and twelfth rows to give spatial averages representative of one complete period of dimple surface geometry. This particular period extends over X/D from 8.00 to 9.52 and over Z/D from +0.81 to −0.81.

The first three data sets listed in the legend of Fig. 9, and given in Figs. 9 and 10, are obtained with a smooth top wall and with top walls with protrusions arranged in configurations 1 and 2. With configuration 1 or full offset configuration, the dimples and protrusions are misaligned, and with configuration 2 no offset is employed, and dimples and protrusions are exactly aligned with each other. These three sets are all for about the same Reynolds number ($Re_H = 10.2 \times 10^3$–10.6×10^3) and temperature ratio ($T_{oi}/T_w = 0.92$–0.94). In each case, low Nusselt-number ratios correspond with upstream portions of the dimple cavities, and the highest ratios are from locations near the side rims or near the downstream edges of the dimples. The most important differences between the three data sets are significantly higher $\overline{Nu}/Nu_0$ at most all values of X/D and Z/D when the protrusions are employed. However, in spite of these differences, the peaks and valleys of the $\overline{Nu}/Nu_0$ distributions roughly cover the same ranges of locations. Differences in locations and shapes of $\overline{Nu}/Nu_0$ in these regions are caused by the actions of the protrusions in influencing the development of secondary flows from different dimples. Pressure distributions in the flow are altered significantly as the protrusions are added or their locations are changed. This then alters the emergence and development of the vortical mixing fluid from dimples as it enhances heat transfer near downstream edges and spanwise edges of dimples. The largest changes to $\overline{Nu}/Nu_0$ distributions from such phenomena are apparent in Fig. 9 at X/D from 8.2 to 9.2.

The next data set in Figs. 9 and 10 is measured at a Reynolds number Re_H of 3.5×10^4 with protrusions on the top wall arranged in configuration 2 with $T_{oi}/T_w = 0.94$. When compared to the data

	Top Wall	Configuration	Offset	T_{oi}/T_w
●	Smooth[1]	—	—	0.92-0.94
◇	Protrusions	1	Full offset (Misaligned)	0.92-0.94
□	Protrusions	2	No offset (Aligned)	0.93-0.94

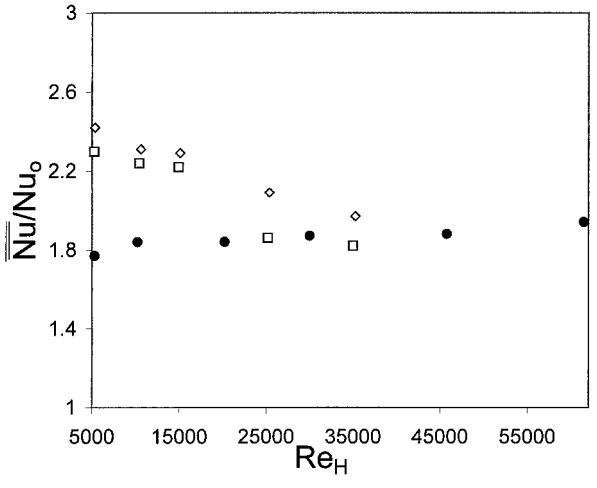

Fig. 11 Globally averaged Nusselt-number ratios as dependent on Reynolds number Re_H for approximately constant temperature ratio, T_{oi}/T_w.

set obtained with similar geometry and flow parameters, but at a lower Re_H of 10.4×10^3, it is evident that spatially averaged $\overline{Nu}/Nu_0$ decrease significantly at each spatial location as Re_H increases from 10.4×10^3 to 3.5×10^4. Differences are most apparent at locations near local maxima in $\overline{Nu}/Nu_0$ distributions. Variations with X/D and Z/D are also somewhat smaller overall when $Re_H = 3.5 \times 10^4$ than when $Re_H = 10.4 \times 10^3$.

Spatially averaged $\overline{Nu}/Nu_0$ distributions for two temperature ratios (T_{oi}/T_w of 0.93 and 0.78) at constant Re_H (of 10.4×10^3 and 13.2×10^3) with the same configuration 2 protrusion top wall arrangement are now compared. Figures 9 and 10 show that the spatially averaged values increase significantly at all X/D and Z/D locations as T_{oi}/T_w decreases. Such changes near $\overline{Nu}/Nu_0$ local maxima are mostly because of higher Nu/Nu_0 values just downstream of dimples or near diagonal positions of the dimples where unsteady vortical motions have the most pronounced effects. Here, variable property effects and buoyancy augment the actions of the vortices in advecting different sized packets of cold mainstream fluid to regions near the hot walls.

E. Globally Averaged Nusselt Numbers and Friction Factors

Globally averaged $\overline{\overline{Nu}}/Nu_0$ are determined by averaging local Nusselt number ratios over a measurement area corresponding to one complete pattern of dimple test surface. This is the same portion of the test surface used to obtained the spatially averaged Nusselt-number data.

Figure 11 gives distributions of globally averaged data vs Re_H at a constant temperature ratio of 0.92–0.94. Data obtained with a smooth top wall, and with two different arrangements of the protrusion top wall (configurations 1 and 2), are included. Globally averaged values increase very slightly (and are nearly constant) with Re_H when a smooth top wall is employed. $\overline{\overline{Nu}}/Nu_0$ are higher when protrusions are employed on the top wall for $Re_H < 4 \times 10^4$ and about the same for $Re_H > 4 \times 10^4$. $\overline{\overline{Nu}}/Nu_0$ measured with protrusions on the top wall thus generally decrease as Reynolds

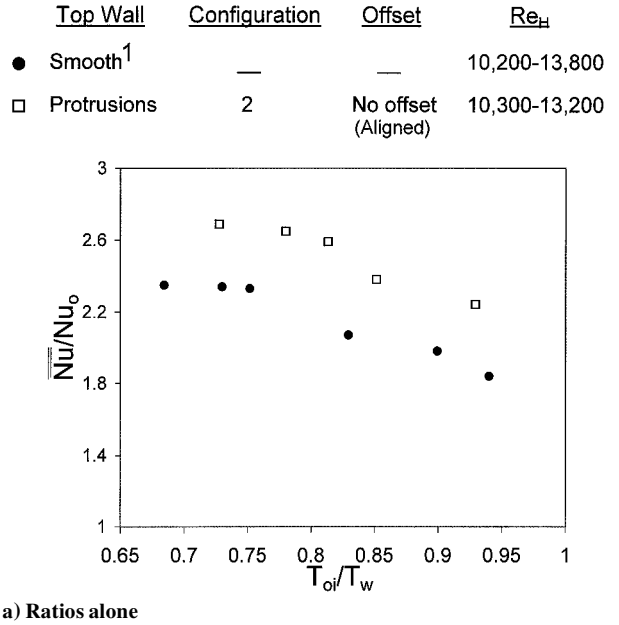

a) Ratios alone

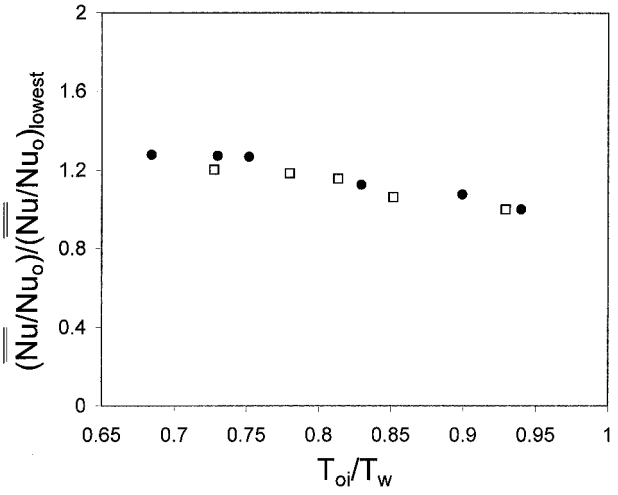

b) Ratios normalized by lowest measured Nusselt-number ratio

Fig. 12 Globally averaged Nusselt-number ratios as dependent on T_{oi}/T_w, for approximately constant Reynolds number Re_H.

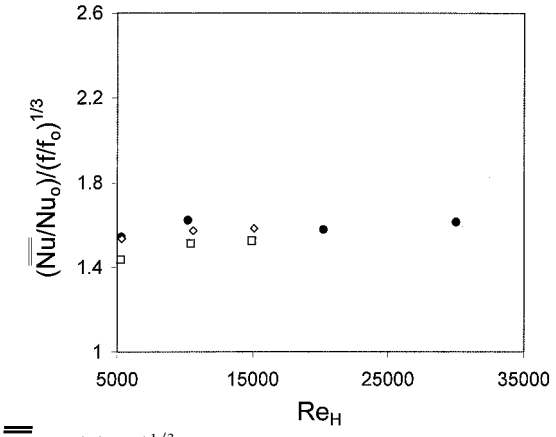

a) $(\overline{\overline{Nu}}/Nu_0)/(f/f_0)^{1/3}$ values based on total area of the test surface (flat regions and indented dimple regions)

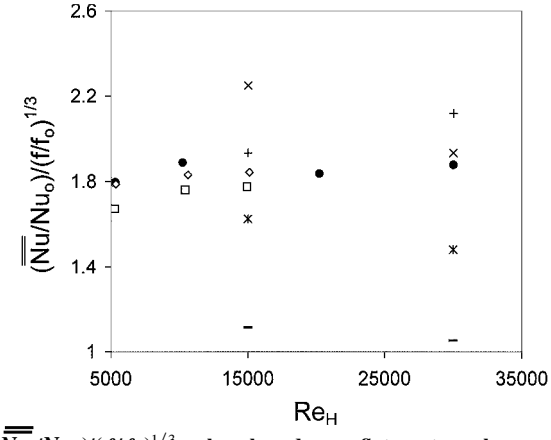

b) $(\overline{\overline{Nu}}/Nu_0)/(f/f_0)^{1/3}$ values based on a flat, rectangular projected area

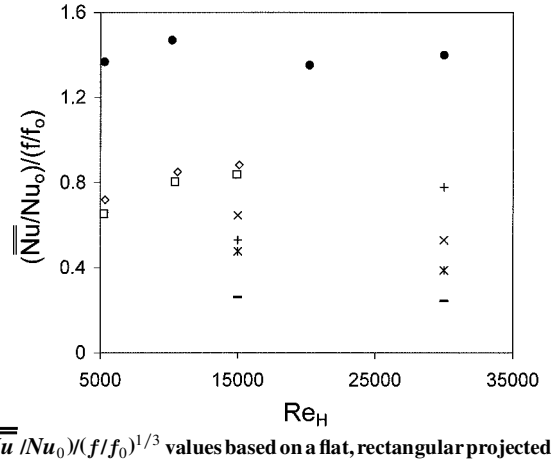

c) $(\overline{\overline{Nu}}/Nu_0)/(f/f_0)^{1/3}$ values based on a flat, rectangular projected area

Fig. 13 Performance parameter magnitudes as dependent on Reynolds number Re_H for approximately constant temperature ratio T_{oi}/T_w: ×, 60° V-shaped broken rib;[18] +, 60° broken rib;[18] *, delta-shaped forward aligned rib;[18] and –, wedge-shaped continuous rib.[18] Other symbols are identified in Fig. 11.

number increases, changing about 20% as Re_H ranges from 5×10^3 to 4×10^4. Thus, the dimple-protrusion surface arrangement gives $\overline{Nu}/Nu_0$ with greater Reynolds-number dependence than the dimple-smooth surface arrangement, as mentioned. $\overline{Nu}/Nu_0$ are slightly higher with configuration 1 protrusions than with configuration 2 protrusions when compared at the same Re_H, provided Re_H is less than 4×10^4.

Figure 12a presents globally averaged $\overline{Nu}/Nu_0$ distributions as dependent upon T_{oi}/T_w for approximately constant Reynolds number. The Nu_0 values used for normalization are measured at T_{oi}/T_w of 0.92–0.94. Notice that ratios from Mahmood et al.[1] for a smooth top wall are lower than ratios measured with the configuration 2 protrusion top wall, when compared at the same T_{oi}/T_w. As T_{oi}/T_w decreases over the range shown, $\overline{Nu}/Nu_0$ values increase by about 28% when a smooth top wall is employed and by about 18% when a protrusion top wall is used.

The data given in Fig. 12a are again presented in Fig. 12b, after normalization using the $\overline{Nu}/Nu_0$ ratio at $T_{oi}/T_w = 0.92 - 0.94$. This arrangement is used to provide additional insight into the dependence of the $\overline{Nu}/Nu_0$ data on T_{oi}/T_w. The two different data sets in the figure show about the same dependence on T_{oi}/T_w, both with and without protrusions on the top wall.

Magnitudes of $(\overline{Nu}/Nu_0)/(f/f_0)^{1/3}$, the thermal performance parameter,[17] are given in Figs. 13a and 13b for the channel with the smooth top wall and two different arrangements of the protrusion top wall. Friction factor data used for this determination are given in Fig. 14. Normalized friction factors from a protrusion-dimple channel are much higher than values from a smooth-dimple channel. In Fig. 13a heat transfer coefficients used to deduce the Nusselt numbers are based on the total area of the test surface (flat regions and indented dimple regions). In Fig. 13b heat transfer coefficients are presented, which are based on a flat, rectangular projected area. The difference in values based on these two different reference areas is 16.4%.

Data compared over the same T_{oi}/T_w range (0.92–0.94) in Fig. 13a show that the thermal performance parameter with the smooth top wall are nearly constant as Re_H changes, ranging from 1.55 to 1.60. As such, these values are slightly higher than values obtained with protrusions on the top wall, which range from 1.45 to about 1.55, and appear to increase slightly with Reynolds number. The lower performance parameter values obtained with protrusions on the top wall are caused by the large increases in f/f_0 caused by protrusion form drag. Such behavior indicates slight disadvantages when protrusions are employed on the top surface of the dimpled channel. Using the protrusions is thus advantageous only when $\overline{Nu}/Nu_0$ values are considered alone, and relatively low pressure drops and friction factor magnitudes are not required or are not important in the intended application.

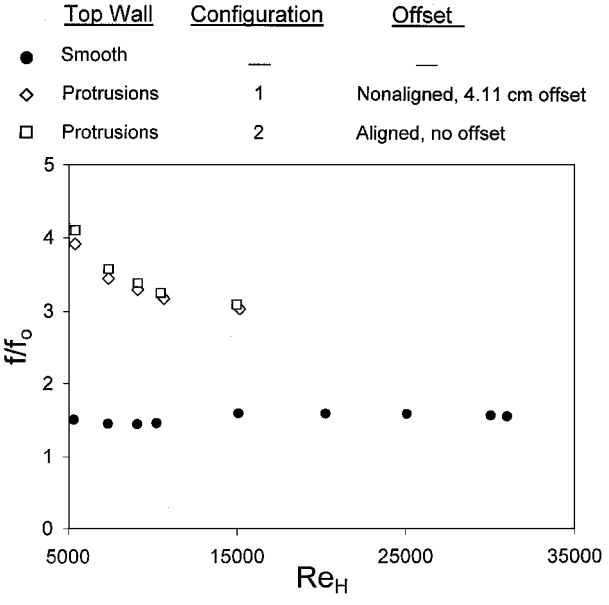

Fig. 14 Normalized channel friction factors as dependent on Reynolds number.

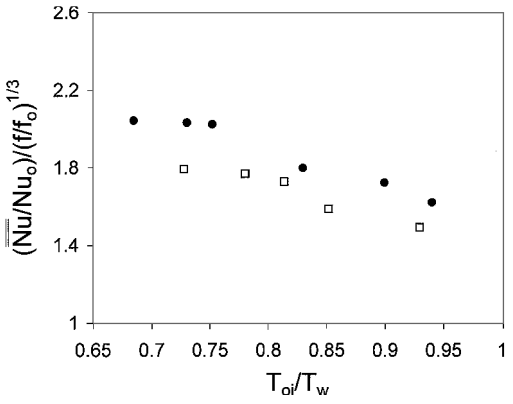

a) Values based on total area of the test surface (flat regions and indented dimple regions)

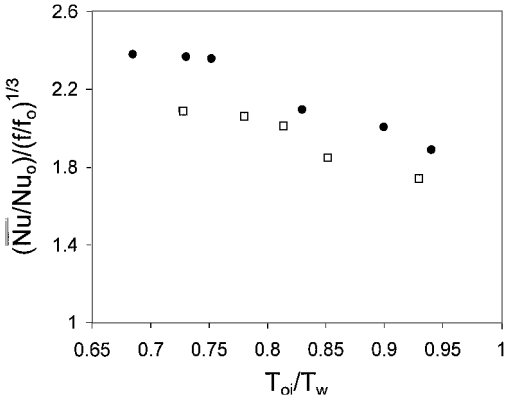

b) Values based on a flat, rectangular projected area

Fig. 15 Performance parameter magnitudes as dependent on T_{oi}/T_w for approximately constant Reynolds number Re_H. Symbols identified in Fig. 12.

Figure. 13b shows that the performance parameters from the dimple-smooth channel and from the dimple-protrusion channel lie in the middle of the range of data for several rib turbulator arrangements from Han et al.[18] However, a different conclusion is reached if the $(\overline{Nu}/Nu_0)/(f/f_0)$ performance parameters, shown in Fig. 13c, are considered. In this case the present data are higher than all rib-turbulator data sets from Han et al.[18]

Performance parameter magnitudes as dependent upon T_{oi}/T_w, for approximately constant Reynolds number Re_H, are presented in Figs. 15a and 15b. Values in the first of these figures are based on total area of the test surface (flat regions and indented dimple regions), whereas values in the second figure are based on a flat, rectangular projected area. Again, as for the preceding figures, it is evident that values with a smooth top surface are slightly higher than values determined with protrusions on the top wall.

IV. Conclusions

Local and spatially averaged Nusselt-number data, and thermal performance parameters, are presented for the dimpled surface of a channel, both with and without protrusions (with the same shapes as the dimples) on the opposite wall. Channel aspect ratio is 16, ratio of channel height to dimple print diameter is 0.5, Reynolds numbers based on channel height ranges from 5×10^3 to 3.5×10^4, and ratio of channel inlet stagnation temperature to wall temperature ranges from 0.73 to 0.94.

The protrusions result in additional shedding of vortical, secondary flow structures from the dimples, as well as increased flow unsteadiness. As a result, local, spanwise-averaged, and streamwise-averaged Nusselt numbers are augmented considerably, and have

greater Reynolds-number dependence, compared to a channel with a smooth top wall and dimples on one opposite wall. Local and spatially averaged Nusselt-number variations are also observed as the location of the array of protrusions is changed with respect to the dimples. Such changes are particularly apparent at locations near local maxima in Nusselt-number ratio distributions, and near downstream edges and spanwise edges of dimples. In the upstream portions of the dimple cavities, local Nusselt-number ratios decrease somewhat when protrusions are added to the top surface. Important alterations with T_{oi}/T_w are also observed, principally because of the added contributions of variable property effects and buoyancy. As this temperature ratio decreases, parts of the test surface with the highest values of Nu/Nu_0 intensify, broaden, and extend farther away from the downstream rims of the dimples.

Globally averaged $\overline{\overline{Nu}}/Nu_0$, measured with protrusions on the top wall, generally decrease as Reynolds number increases, changing about 20% as Re_H ranges from 5×10^3 to 4×10^4. The dimple-protrusion surface arrangement thus gives $\overline{\overline{Nu}}/Nu_0$ with greater Reynolds-number dependence than the dimple-smooth surface arrangement. $\overline{\overline{Nu}}/Nu_0$ magnitudes are also slightly higher when the protrusions and dimples are misaligned (configuration 1) than when the protrusions and dimples are aligned (configuration 2), when compared at the same Re_H (provided $Re_H < 4 \times 10^4$).

Magnitudes of the thermal performance parameter $(\overline{\overline{Nu}}/Nu_0)/(f/f_0)^{1/3}$, measured with protrusions on the top wall, range from 1.45 to about 1.55, and increase slightly with Reynolds number. Like the $\overline{\overline{Nu}}/Nu_0$ data, performance parameter magnitudes increase as the temperature ratio T_{oi}/T_w decreases (for approximately constant Reynolds number Re_H), both with and without protrusions on the channel top wall. In both cases values with a smooth top surface are slightly higher than values determined with protrusions on the top wall because of the large friction factor increases caused by protrusion form drag.[2] This means that using the protrusions is advantageous only when $\overline{\overline{Nu}}/Nu_0$ values and heat transfer augmentations are considered alone, and relatively low pressure drops and friction factor magnitudes are not needed in the application of interest.

Acknowledgments

The work presented in this paper was performed as a part of the Advanced Turbine System Technology Development Project, sponsored both by the U.S. Department of Energy and Solar Turbines, Inc. Hee-Koo Moon and Boris Glezer, both of Solar Turbines, Inc., are acknowledged for useful discussions on the research.

References

[1] Mahmood, G. I., Hill, M. L., Nelson, D. L., Ligrani, P. M., Moon, H.-K., and Glezer, B., "Local Heat Transfer and Flow Structure on and Above a Dimpled Surface in a Channel," *Journal of Turbomachinery*, Vol. 123, No. 1, 2001, pp. 115–123.

[2] Ligrani, P. M., Mahmood, G. I., Nelson, D. L., Harrison, J. L., and Clayton, C. M., "Flow Structure and Local Nusselt Number Variations in a Channel with Dimples and Protrusions on Opposite Walls," *International Journal of Heat and Mass Transfer*, Vol. 44, No. 23, 2001.

[3] Afanasyev, V. N., Chudnovsky, Y. P., Leontiev, A. I., and Roganov, P. S., "Turbulent Flow Friction and Heat Transfer Characteristics for Spherical Cavities on a Flat Plate," *Experimental Thermal and Fluid Science*, Vol. 7, No. 1, 1993, pp. 1–8.

[4] Belen'kiy, M. Y., Gotovskiy, M. A., Lekakh, B. M., Fokin, B. S., and Dolgushin, K. S., "Heat Transfer Augmentation Using Surfaces Formed by a System of Spherical Cavities," *Heat Transfer Research*, Vol. 25, No. 2, 1994, pp. 196–203.

[5] Kesarev, V. S., and Kozlov, A. P., "Convective Heat Transfer in Turbulized Flow Past a Hemispherical Cavity," *Heat Transfer Research*, Vol. 25, No. 2, 1994, pp. 156–160.

[6] Terekhov, V. I., Kalinina, S. V., and Mshvidobadze, Y. M., "Flow Structure and Heat Transfer on a Surface with a Unit Hole Depression," *Russian Journal of Engineering Thermophysics*, Vol. 5, 1995, pp. 11–33.

[7] Schukin, A. V., Koslov, A. P., and Agachev, R. S., "Study and Application of Hemispherical Cavities for Surface Heat Transfer Augmentation," American Society of Mechanical Engineers, Paper 95-GT-59, June 1995.

[8] Gortyshov, Y. F., Popov, I. A., Amirkhanov, R. D., and Gulitsky, K. E., "Studies of Hydrodynamics and Heat Exchange in Channels with Various Types of Intensifiers," *Proceedings of 11th International Heat Transfer Congress*, Vol. 6, Taylor and Francis, Philadelphia, PA, 1998, pp. 83–88.

[9] Chyu, M. K., Yu, Y., Ding, H., Downs, J. P., and Soechting, F. O., "Concavity Enhanced Heat Transfer in an Internal Cooling Passage," American Society of Mechanical Engineers, Paper 97-GT-437, June 1997.

[10] Lin, Y.-L., Shih, T. I.-P., and Chyu, M. K., "Computations of Flow and Heat Transfer in a Channel with Rows of Hemispherical Cavities," American Society of Mechanical Engineers, Paper 99-GT-263, June 1999.

[11] Moon, H.-K., O'Connell, T., and Glezer, B., "Channel Height Effect on Heat Transfer and Friction in a Dimpled Passage," American Society of Mechanical Engineers, Paper 99-GT-163, June 1999.

[12] Sargent, S. R., Hedlund, C. R., and Ligrani, P. M., "An Infrared Thermography Imaging System for Convective Heat Transfer Measurements in Complex Flows," *Measurement Science and Technology*, Vol. 9, No. 12, 1998, pp. 1974–1981.

[13] Hedlund, C. R., and Ligrani, P. M., "Local Swirl Chamber Heat Transfer and Flow Structure at Different Reynolds Numbers," *Journal of Turbomachinery*, Vol. 122, No. 2, 2000, pp. 375–385.

[14] Moffat, R. J., "Describing the Uncertainties in Experimental Results," *Experimental Thermal and Fluid Science*, Vol. 1, No. 1, 1988, pp. 3–17.

[15] Kays, W. M., and Crawford, M. E., *Convective Heat and Mass Transfer*, 3rd ed., McGraw–Hill, New York, 1993.

[16] Han, J. C., Park, J. S., and Lei, C. K., "Heat Transfer Enhancement in Channels with Turbulence Promoters," *Journal of Heat Transfer*, Vol. 107, No. 3, 1985, pp. 628–635.

[17] Gee, D. L., and Webb, R. L., "Forced Convection Heat Transfer in Helically Rib-Roughened Tubes," *International Journal of Heat and Mass Transfer*, Vol. 23, No. 8, 1980, pp. 1127–1136.

[18] Han, J.-C., Huang, J. J., and Lee, C. P., "Augmented Heat Transfer in Square Channels with Wedge-Shaped and Delta-Shaped Turbulence Promoters," *Enhanced Heat Transfer*, Vol. 1, No. 1, 1993, pp. 37–52.